Geoscientific Model Development

Supporting Information for

EarthMesh: A Multi-scale Unstructured Mesh Generation Tool for Earth System Models

Rui Zhang[1], Zhongwang Wei[1*], Yinhai Luo[2], Hanwen Fan[3], Qingchen Xu[1], Shupeng Zhang[1], Nan Wei[1], Xingjie Lu[1], Lu Li[1], Huan Yuan[1], Xianxiang Li[1], Shaofeng Liu[1], Wei Shangguan[1], Yongjiu Dai[1*]

[1]School of Atmospheric Sciences, Sun Yat-sen University, Zhuhai, China

[2]Laboratory of Middle Atmosphere and Global Environment Observation, Institute of Atmospheric Physics, Chinese Academy of Sciences, Beijing, China

[3]Commercial Aircraft Corporation of China Ltd Meteorological Research Center, Commercial Aircraft Corporation of China Ltd Shanghai Aircraft Flight Test Co., Ltd., Shanghai, China

Correspondence to: Zhongwang Wei (weizhw6@mail.sysu.edu.cn); Yongjiu Dai (daiyj6@mail.sysu.edu.cn)

Contents of this file

Texts S1 to S3
Figures S1 to S6
Tables S1 to S5

Text S1. Atmospheric experiment design

All atmospheric runs follow the initial conditions of Jablonowski and Williamson (2006). In general, the baroclinic wave starts growing observably around day 4 and evolves rapidly thereafter with explosive cyclogenesis at model day 8. The spread of the numerical solutions increases noticeably from model day 12 onwards. This indicates the predictability limit of the test case (Jablonowski and Williamson, 2006). Therefore, all atmospheric runs integrate for 17 model days, but output only from the first 12 model days are analyzed. All simulations reported here used a time step of 120 s, regardless of horizontal grid spacing, to facilitate intercomparison and interpretation. Simulated surface pressure and 850 hPa relative vorticity are evaluated against high-resolution reference solution (A2, **Table 1**) with Root Mean Square Error (RMSE). RMSE is calculated as

$$RMSE = \sqrt{\frac{1}{N}\sum_{i=1}^{N}\left(X_{i,sim} - X_{i,ref}\right)^2} \quad (1)$$

where $X_{i,ref}$ is the high-resolution reference solution, and $X_{i,sim}$ represents the simulated values from other resolution modeling. Subscript i denotes the ith grid, n is the total number of the grids.

Text S2. Oceanic experiment design

The oceanic experiments use an two-dimensional idealized geostrophic eddy test. The initial field (φ, u, v) of the geostrophic vortex from Eqs. (2-4), with the maximum velocity (V_{max}) at 0.5 m/s, appearing at 120 km away from the eddy center (28.5°N, 128.5°E).

$$\varphi(x,y) = -\frac{RfV_{max}}{g}\frac{\sqrt{e}}{2}\exp\left(-\frac{r^2}{R^2}\right) \quad (2)$$

$$u(x,y) = -V_{max}\frac{r}{R}\exp\left(\frac{1}{2}\left(1--\frac{r^2}{R^2}\right)\right)\sin\left(atan2(y,x)+\frac{\pi}{2}\right) \quad (3)$$

$$v(x,y) = -V_{max}\frac{r}{R}\exp\left(\frac{1}{2}\left(1--\frac{r^2}{R^2}\right)\right)\cos\left(atan2(y,x)+\frac{\pi}{2}\right) \quad (4)$$

Where R is constant 120 km. r denotes the distance from the eddy center, while x and y are position coordinates relative to it. The model domain uses a single layer with a constant depth of 2000 m. Closed boundary conditions are applied at the lateral boundaries of the model domain. All runs start on the spherical coordinates and integrate for 10 model days, with the Coriolis parameter depending on the latitude of the eddy center. The model avoids applying bottom friction to better maintain vortex characteristics. We use the Smagorinsky scheme with a parameter of 0.1 in the horizontal direction. All simulations reported here used a barotropic time step of 20 s, regardless of horizontal grid spacing. Simulated velocity fields are evaluated against high-resolution reference solution (O2, **Table 2**) with Root Mean Square Error (RMSE).

Text S3. Land-surface experiment design

All land-surface simulations are driven by hourly ERA5-Land forcing (Muñoz-Sabater et al., 2021) and run from 2001 to 2010 with the same time step of 1800 s. The first five years are spin-up, and the monthly output from 2006 to 2010 is analyzed. Simulated runoff is evaluated against the Global Reach-level Flood Reanalysis (GRFR) dataset (Yang et al., 2021) with the Kling-Gupta Efficiency (KGE) Skill Score (KGESS; Gupta et al., 2009; Knoben et al., 2019). KGESS and

KGE are calculated as

$$KGESS = \frac{KGE_{sim} - KGE_{bench}}{1 - KGE_{bench}} \quad (5)$$

$$KGE = 1 - \sqrt{(r-1)^2 + (\alpha-1)^2 + (\beta-1)^2} \quad (6)$$

where KGE_{sim} is the KGE value from the CoLM2024 simulation evaluated against the validation dataset, and KGE_{bench} = -0.41 is the KGE value of the observed-mean-flow benchmark against observations (Knoben et al., 2019). KGESS ranges from -∞ to 1, and higher values indicate better performance. r is the Pearson correlation coefficient, α is the relative variability, β is the bias ratio. **Table S4** lists the datasets used for mesh refinement, surface properties, forcing, and validation.

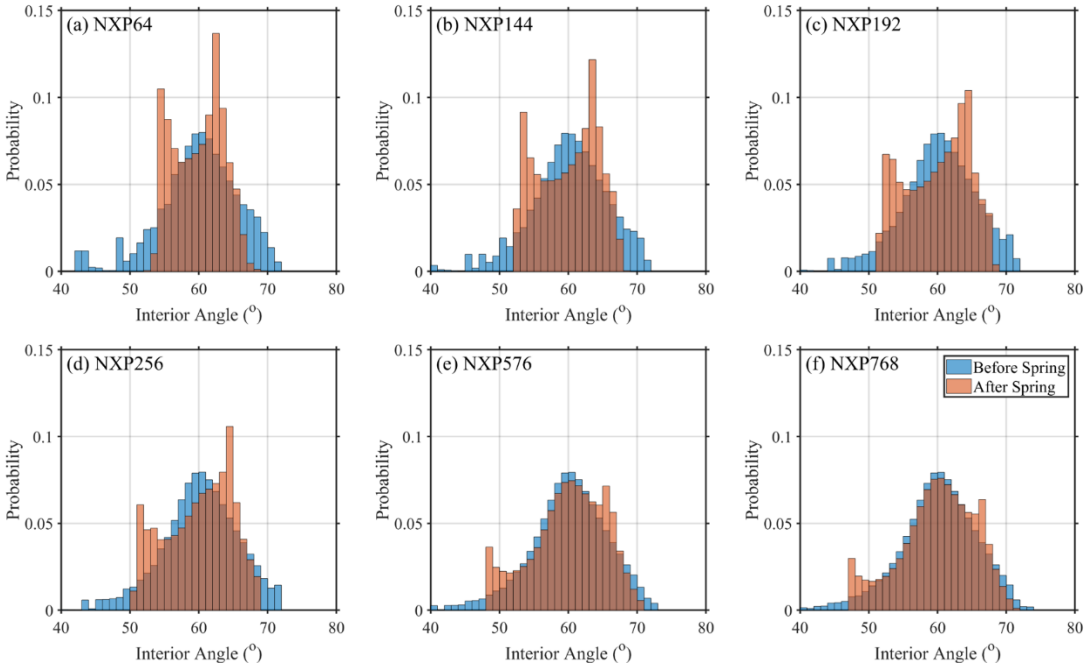


Figure S1. Interior-angle distributions of triangular cells in six quasi-uniform meshes (a) NXP64, (b) NXP144, (c) NXP192, (d) NXP256, (e) NXP576, and (f) NXP768 before and after spring adjustment. All three interior angles of each cell are included.

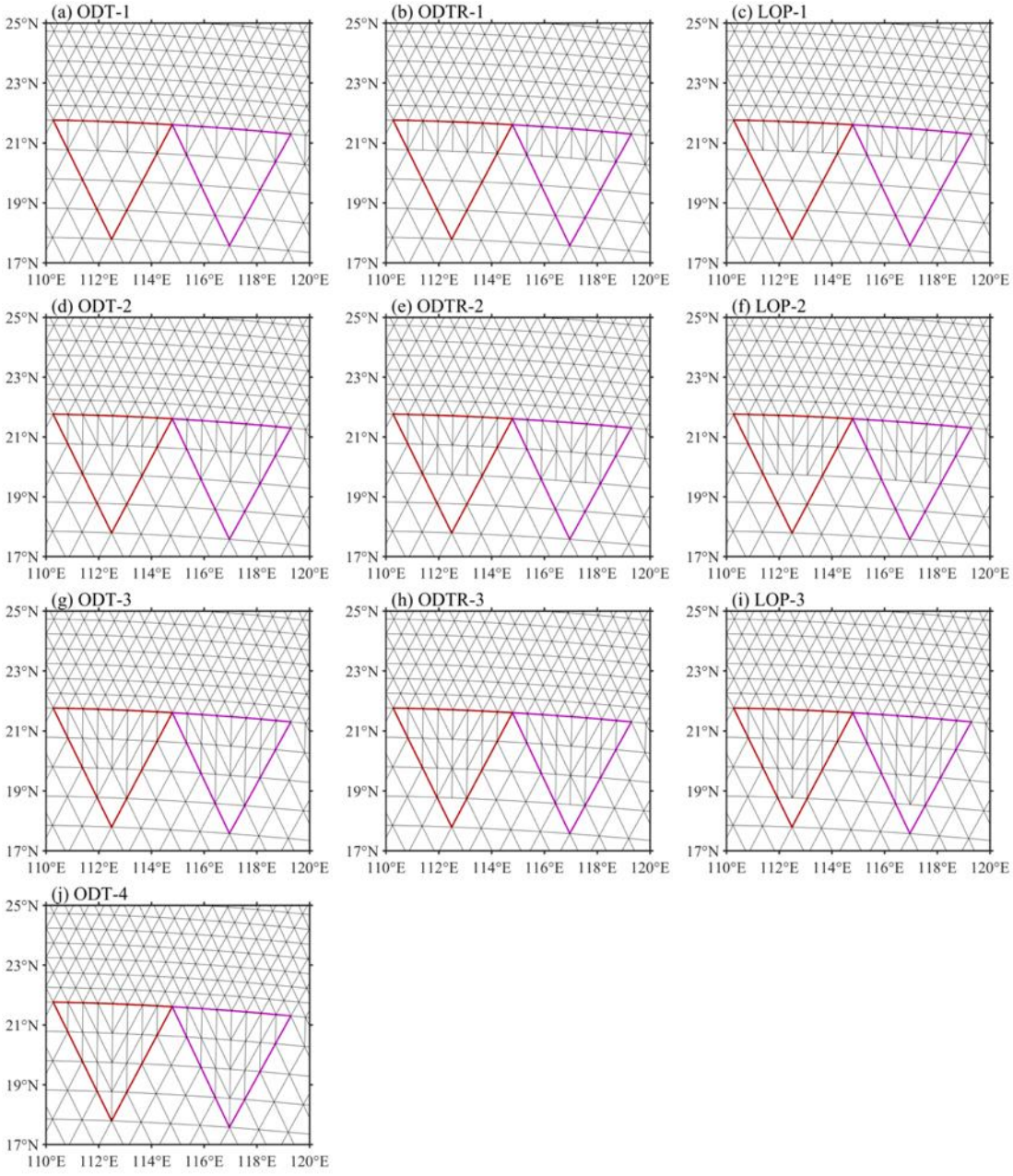


Figure S2. Construction of transition rows outside a refinement region without weak concavity for M = 4. M refers to the number of transition rows. Each set of M adjacent hanging nodes forms a triangular color group. ODT: One triangle divides into two small triangles; ODTR: Reverse ODT; LOP: Local Optimization Procedure, means that exchange the two diagonals of a convex quadrilateral composed of two triangles.

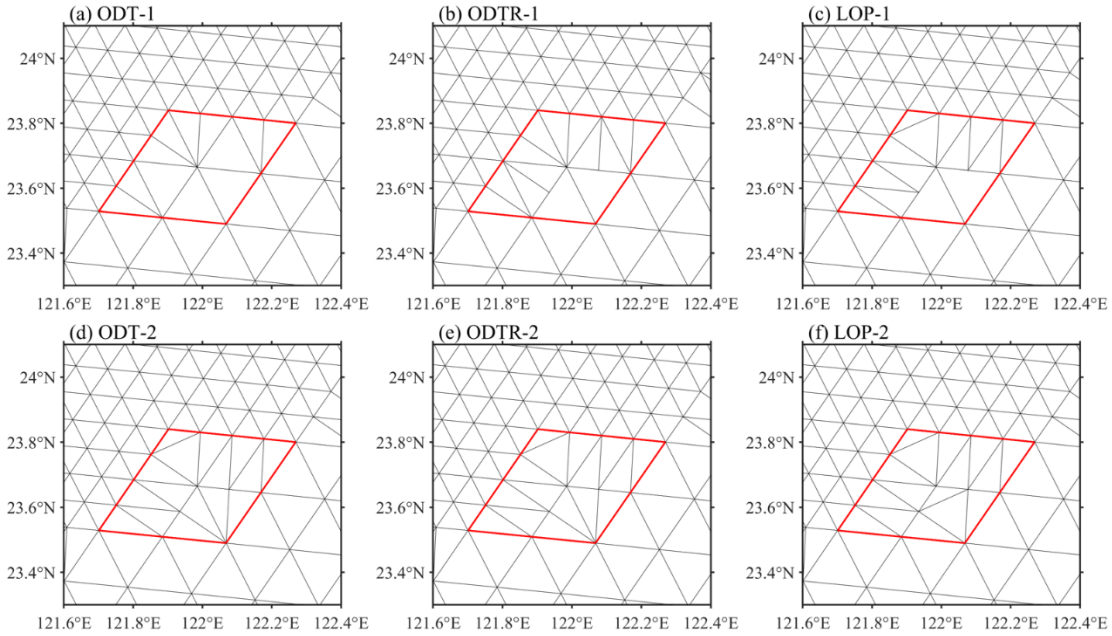


Figure S3. Construction of transition rows outside a refinement region with weak concavity using M = 2. Two adjacent triangular color groups merge into a quadrilateral group. Subgraphs (d) and (e) illustrate that ODTR-2 does not modify the grid connection for M = 2.

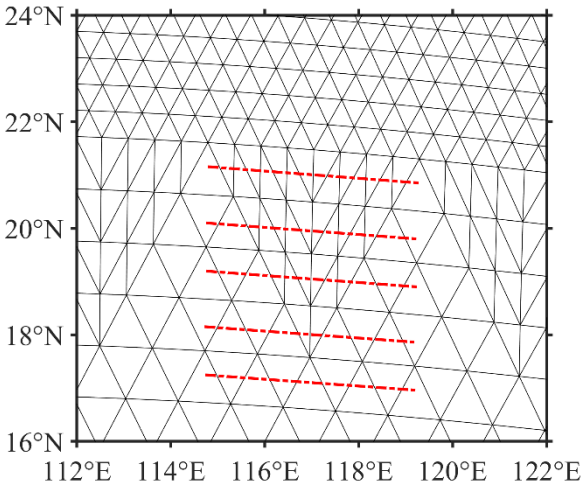


Figure S4. Equilibrium spring length within the transition zone for a variable-resolution mesh. The Red lines indicates that the equilibrium length located in the resolution transition region needs to change linearly.

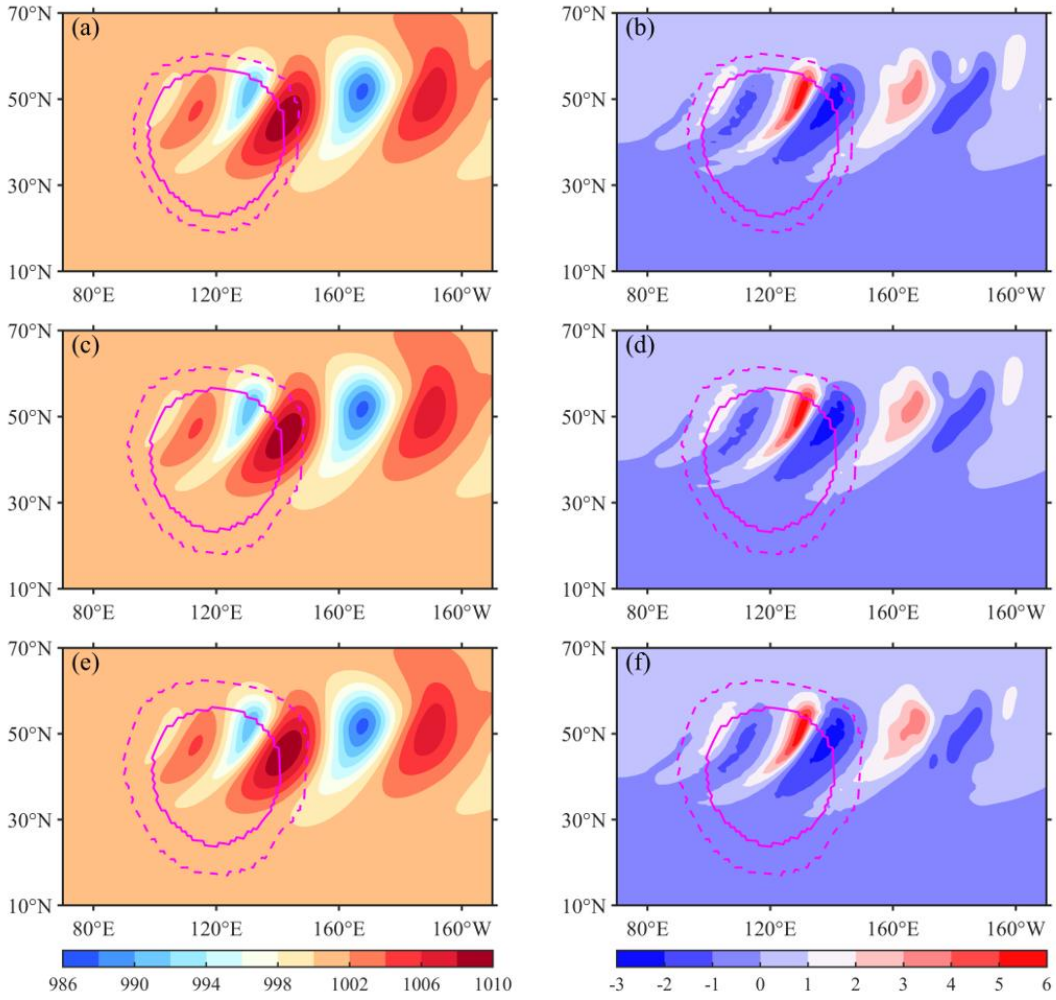


Figure S5. Surface pressure (hPa, left column) and 850 hPa relative vorticity (10^{-5} s^{-1}, right column) for experiments A-R2M2 (a, b), A-R2M3 (c, d), A-R2M4 (e, f) after 7 model days. Purple solid and dashed lines mark the approximate 30 km and 120 km mesh-spacing boundaries, respectively.

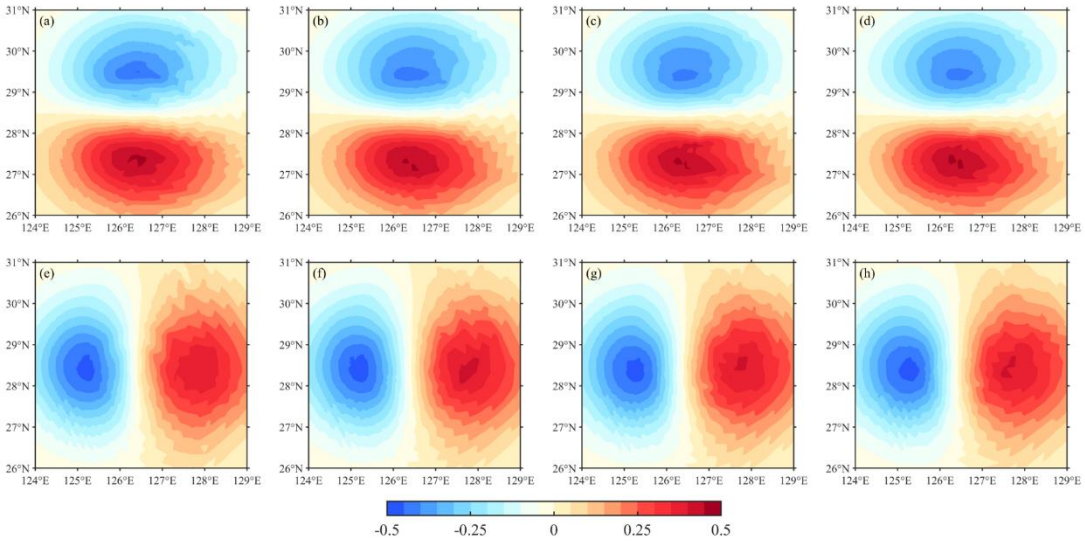


Figure S6. Eastward surface velocity (m s^{-1}, top row) and northward surface velocity (m s^{-1}, bottom row) for xperiments O-R2M1 (a, e), O-R2M2 (b, f), O-R2M3 (c, g), O-R2M4 (d, h) after 10 model days.

Table S1. Statistical characteristics of the interior angle distribution of triangular cells for quasi-uniform meshes before and after spring dynamics adjustment (Tomita et al., 2002). The interior angle distribution is binned into six categories. $P_{50\text{-}60}$ denotes the percentage (%) of interior angles falling between 50° and 60°. The other five categories are defined analogously, and Min/Max denotes the minimum and maximum interior angles. *-Before denote meshes generated before spring dynamics adjustment

ID	Min/Max (°)	$P_{<40}$	$P_{40\text{-}50}$	$P_{50\text{-}60}$	$P_{60\text{-}70}$	$P_{70\text{-}80}$	$P_{>80}$
NXP64-Before	42.91/72.00	0.000	5.420	41.968	50.684	1.929	0.000
NXP144-Before	39.88/72.00	0.725	4.146	42.664	49.900	2.566	0.000
NXP192-Before	38.82/72.00	0.811	4.462	42.240	49.640	2.846	0.000
NXP256-Before	37.80/72.00	0.670	4.582	42.261	49.770	2.717	0.000
NXP576-Before	35.03/73.00	0.329	4.889	42.309	50.054	2.419	0.000
NXP768-Before	34.09/73.70	0.448	4.717	42.363	50.026	2.446	0.000
NXP64	52.99/72.00	0.000	0.000	46.897	53.079	0.024	0.000
NXP144	52.60/72.00	0.000	0.000	46.249	53.746	0.005	0.000
NXP192	51.79/72.00	0.000	0.000	45.613	54.384	0.003	0.000
NXP256	50.93/72.00	0.000	0.000	45.332	54.667	0.002	0.000
NXP576	48.09/72.00	0.000	6.106	40.149	53.184	0.562	0.000
NXP768	47.01/72.01	0.000	6.680	39.929	52.638	0.754	0.000

* NXP serves as the resolution parameter. NXP = 64/144/192/256/576/768 indicates the average horizontal spacing of about 120/53.3/40/30/13.3/10 km, respectively.

Table S2. Same as Table S1, but for atmospheric variable-resolution meshes. A-R2Mn-Before denote meshes generated before spring dynamics adjustment; A-R2Mn denote the corresponding meshes after adjustment.

ID	Min/Max (°)	$P_{<40}$	$P_{40\text{-}50}$	$P_{50\text{-}60}$	$P_{60\text{-}70}$	$P_{70\text{-}80}$	$P_{>80}$
A-R2M1-Before	26.40/124.76	0.204	0.000	46.167	53.424	0.018	0.188
A-R2M2-Before	26.20/124.77	0.411	0.000	45.984	53.200	0.018	0.386
A-R2M3-Before	26.42/124.80	0.484	0.000	45.942	53.095	0.018	0.460
A-R2M4-Before	26.29/124.81	0.539	0.000	45.925	53.003	0.019	0.514
A-R2M1	29.00/90.15	0.154	0.405	46.138	52.620	0.619	0.064
A-R2M2	33.45/87.65	0.059	0.590	46.284	52.369	0.657	0.040
A-R2M3	35.43/85.64	0.015	0.581	46.526	52.190	0.657	0.031
A-R2M4	36.52/86.07	0.010	0.574	46.723	51.966	0.694	0.034

157

158

159 **Table S3.** Same as Table S2, but for oceanic variable-resolution meshes.

ID	Min/Max (°)	$P_{<40}$	$P_{40\text{-}50}$	$P_{50\text{-}60}$	$P_{60\text{-}70}$	$P_{70\text{-}80}$	$P_{>80}$
O-R2M1-Before	25.86/127.28	0.425	0.000	37.689	61.509	0.000	0.377
O-R2M2-Before	25.88/127.32	0.870	0.000	37.073	61.263	0.000	0.795
O-R2M3-Before	25.84/127.33	0.924	0.000	36.824	61.401	0.000	0.850
O-R2M4-Before	25.88/127.37	0.981	0.000	36.815	61.304	0.000	0.900
O-R2M1	28.68/90.43	0.232	1.018	38.484	58.831	1.266	0.170
O-R2M2	36.04/88.66	0.038	1.392	39.536	57.489	1.419	0.127
O-R2M3	36.96/87.22	0.012	1.282	41.493	55.785	1.310	0.118
O-R2M4	36.28/89.57	0.037	1.342	43.171	53.784	1.502	0.164

160

161

162 **Table S4**. Datasets used for mesh construction, land surface property construction, model forcing, and
163 model validation in the land surface experiments.

Datasets	Spatial resolution	Temporal resolution	Source and reference
Dataset for mesh construction			
Land cover types	1/240°	Invariant	MODIS MCD12Q1 Version 6.1 (Friedl and Sulla-Menashe , 2022)
Leaf area index	1/240°	Invariant	average annual LAI (Lin et al., 2023; Yuan et al., 2011)
Dataset for land surface properties construction			
Land cover types	1/240°	Invariant	MODIS MCD12Q1 Version 6.1 (Friedl and Sulla-Menashe , 2022)
Leaf area index	1/240°	8-day	Improved LAI (Lin et al., 2023; Yuan et al., 2011)
Soil parameters	1/120°	Invariant	SYSU soil dataset (Dai et al., 2019)
Canopy height	10 m	Invariant	Sentinel-2 and GEDI (Lang et al., 2023)
Lake coverage and depth	1/120°	Invariant	GLDB (Kourzeneva et al., 2012)
Model forcing dataset			

Atmospheric forcing Dataset	1/10°	Hourly	ERA5-Land (Muñoz-Sabater et al., 2021)
Model validation datasets			
Runoff dataset	1/10°	Monthly	GRFR (Yang et al., 2021)

Table S5. Comparison with existing unstructured mesh tools.

Tool's Name	Grid Type	Grid refinement method	Include grid post-processing	Model adaptation	Reference
JIGSAW-GEO	Polygonal mesh	User-defined	No	General circulation model	(Engwirda, 2017)
OceanMesh2D	Triangular mesh	physical criteria	Yes	Coastal ocean models	(Roberts et al., 2019)
LandMesh	polygonal mesh	physical criteria	No	Land surface models	(Fan et al., 2024)
OLAM-tools	Triangular/ polygonal mesh	User-defined	No	OLAM model	(Walko and Avissar, 2011)
EarthMesh	Triangular/ polygonal mesh	physical criteria/ User-defined	Yes	Multiple ESM Component	This study

References

Dai, Y., Xin, Q., Wei, N., Zhang, Y., Shangguan, W., Yuan, H., Zhang, S., Liu, S., and Lu, X.: A Global High-Resolution Data Set of Soil Hydraulic and Thermal Properties for Land Surface Modeling, J. Adv. Model. Earth Syst., 11, 2996–3023, https://doi.org/10.1029/2019MS001784, 2019.

Engwirda, D.: JIGSAW-GEO (1.0): locally orthogonal staggered unstructured grid generation for general circulation modelling on the sphere, Geosci. Model Dev., 10, 2117–2140, https://doi.org/10.5194/gmd-10-2117-2017, 2017.

Fan, H., Xu, Q., Bai, F., Wei, Z., Zhang, Y., Lu, X., Wei, N., Zhang, S., Yuan, H., Liu, S., Li, X., Li, X., and Dai, Y.: An Unstructured Mesh Generation Tool for Efficient High-Resolution Representation of Spatial Heterogeneity in Land Surface Models, Geophys. Res. Lett., 51, e2023GL107059, https://doi.org/10.1029/2023GL107059, 2024.

Friedl, M. and Sulla-Menashe, D.: MODIS/Terra+Aqua Land Cover Type Yearly L3

Global 500m SIN Grid V061 [Dataset], NASA Land Processes Distributed Active Archive Center, https://doi.org/10.5067/MODIS/MCD12Q1.061, 2022.

Gupta, H. V., Kling, H., Yilmaz, K. K., and Martinez, G. F.: Decomposition of the mean squared error and NSE performance criteria: Implications for improving hydrological modelling, J. Hydrol., 377, 80–91, https://doi.org/10.1016/j.jhydrol.2009.08.003, 2009.

Jablonowski, C., and Williamson, D. L.: A baroclinic instability test case for atmospheric model dynamical cores, Q. J. Roy. Meteor. Soc., 132, 2943–2975, https://doi.org/10.1256/qj.06.12, 2006.

Knoben, W. J. M., Freer, J. E., and Woods, R. A.: Technical note: Inherent benchmark or not? Comparing Nash–Sutcliffe and Kling–Gupta efficiency scores, Hydrol. Earth Syst. Sci., 23, 4323–4331, https://doi.org/10.5194/hess-23-4323-2019, 2019.

Kourzeneva, E., Asensio, H., and Martin, E.: Global gridded dataset of lake coverage and lake depth for use in numerical weather prediction and climate modelling, Tellus A, 64, 15640, https://doi.org/10.3402/tellusa.v64i0.15640, 2012.

Lang, N., Jetz, W., Schindler, K., and Wegner, J. D.: A high-resolution canopy height model of the Earth, Nat. Ecol. Evol., 7, 1778–1789, https://doi.org/10.1038/s41559-023-02206-6, 2023.

Lin, W., Yuan, H., Dong, W., Zhang, S., Liu, S., Wei, N., Lu, X., Wei, Z., Hu, Y., and Dai, Y.: Reprocessed MODIS Version 6.1 Leaf Area Index Dataset and Its Evaluation for Land Surface and Climate Modeling, Remote Sens., 15, 1780, https://doi.org/10.3390/rs15071780, 2023.

Muñoz-Sabater, J., Dutra, E., Agustí-Panareda, A., Albergel, C., Arduini, G., Balsamo, G., Boussetta, S., Choulga, M., Harrigan, S., Hersbach, H., Martens, B., Miralles, D. G., Piles, M., Rodríguez-Fernández, N. J., Zsoter, E., Buontempo, C., and Thépaut, J.-N.: ERA5-Land: a state-of-the-art global reanalysis dataset for land applications, Earth Syst. Sci. Data, 13, 4349–4383, https://doi.org/10.5194/essd-13-4349-2021, 2021.

Roberts, K. J., Pringle, W. J., and Westerink, J. J.: OceanMesh2D 1.0: MATLAB-based software for two-dimensional unstructured mesh generation in coastal ocean

modeling, Geosci. Model Dev., 12, 1847–1868, https://doi.org/10.5194/gmd-12-1847-2019, 2019.

Tomita, H., Satoh, M., and Goto, K.: An optimization of the icosahedral grid modified by spring dynamics, J. Comput. Phys., 183, 307 – 331, https://doi.org/10.1006/jcph.2002.7193, 2002.

Walko, R. L., and Avissar, R.: A Direct Method for Constructing Refined Regions in Unstructured Conforming Triangular–Hexagonal Computational Grids: Application to OLAM, Mon. Weather Rev., 139, 3923–3937, https://doi.org/10.1175/MWR-D-11-00021.1, 2011.

Yang, Y., Pan, M., Lin, P., Beck, H. E., Zeng, Z., Yamazaki, D., David, C. H., Lu, H., Yang, K., Hong, Y., and Wood, E. F.: Global Reach-Level 3-Hourly River Flood Reanalysis (1980–2019), B. Am. Meteorol. Soc., 102, E2086–E2105, https://doi.org/10.1175/BAMS-D-20-0057.1, 2021.

Yuan, H., Dai, Y., Xiao, Z., Ji, D., and Shangguan, W.: Reprocessing the MODIS Leaf Area Index products for land surface and climate modelling, Remote Sens. Environ., 115, 1171–1187, https://doi.org/10.1016/j.rse.2011.01.001, 2011.